

# Opto-Electronic Science

CN 51-1800/O4 ISSN 2097-0382 (Print) ISSN 2097-4000 (Online)

## Highly sensitive and real-simultaneous CH<sub>4</sub>/C<sub>2</sub>H<sub>2</sub> dual-gas LITES sensor based on Lissajous pattern multi-pass cell

Haiyue Sun, Ying He, Shunda Qiao, Yahui Liu and Yufei Ma

**Citation:** Sun HY, He Y, Qiao SD, et al. Highly sensitive and real-simultaneous CH<sub>4</sub>/C<sub>2</sub>H<sub>2</sub> dual-gas LITES sensor based on Lissajous pattern multi-pass cell. *Opto-Electron Sci* **3**, 240013 (2024).

<https://doi.org/10.29026/oes.2024.240013>

Received: 31 March 2024; Accepted: 24 May 2024; Published online: 28 June 2024

### Related articles

#### A highly sensitive LITES sensor based on a multi-pass cell with dense spot pattern and a novel quartz tuning fork with low frequency

Yahui Liu, Shunda Qiao, Chao Fang, Ying He, Haiyue Sun, Jian Liu, Yufei Ma

*Opto-Electronic Advances* 2024 **7**, 230230 doi: [10.29026/oea.2024.230230](https://doi.org/10.29026/oea.2024.230230)

#### Laser direct writing of Ga<sub>2</sub>O<sub>3</sub>/liquid metal-based flexible humidity sensors

Songya Cui, Yuyao Lu, Depeng Kong, Huayu Luo, Liang Peng, Geng Yang, Huayong Yang, Kaichen Xu

*Opto-Electronic Advances* 2023 **6**, 220172 doi: [10.29026/oea.2023.220172](https://doi.org/10.29026/oea.2023.220172)

#### Optical micro/nanofiber enabled tactile sensors and soft actuators: A review

Lei Zhang, Yuqi Zhen, Limin Tong

*Opto-Electronic Science* 2024 **3**, 240005 doi: [10.29026/oes.2024.240005](https://doi.org/10.29026/oes.2024.240005)

#### Specialty optical fibers for advanced sensing applications

Huanhuan Liu, Dora Juan Juan Hu, Qizhen Sun, Lei Wei, Kaiwei Li, Changrui Liao, Bozhe Li, Cong Zhao, Xinyong Dong, Yuhang Tang, Yihong Xiao, Gerd Keiser, Perry Ping Shum

*Opto-Electronic Science* 2023 **2**, 220025 doi: [10.29026/oes.2023.220025](https://doi.org/10.29026/oes.2023.220025)

More related article in Opto-Electronic Journals Group website 



Opto-Electronic  
Science

<http://www.ojournal.org/oes>



 OE\_Journal



Website

DOI: [10.29026/oes.2024.240013](https://doi.org/10.29026/oes.2024.240013)CSTR: [32246.14.oes.2024.240013](https://cstr.org/cstr/32246.14.oes.2024.240013)

# Highly sensitive and real-simultaneous CH<sub>4</sub>/C<sub>2</sub>H<sub>2</sub> dual-gas LITES sensor based on Lissajous pattern multi-pass cell

Haiyue Sun, Ying He, Shunda Qiao, Yahui Liu and Yufei Ma\*

In this paper, a novel highly sensitive methane (CH<sub>4</sub>) and acetylene (C<sub>2</sub>H<sub>2</sub>) dual-gas light-induced thermoelectric spectroscopy (LITES) sensor based on Lissajous space-division multiplexed (LSDM) technology and trapezoidal-head quartz tuning fork (QTF) detector was reported for the first time. A theoretical LSDM model was established on the basis of three-mirror astigmatic multi-pass cell (MPC) and it was used to design a pair of Lissajous spot patterns with optical path length to volume ratios (OPL/Vs) of 13.5 cm<sup>-2</sup> and 13.3 cm<sup>-2</sup>, respectively. Two self-designed trapezoidal-head QTFs with low resonant frequencies of less than 10 kHz and quality factor of ~12000 were adopted to enhance the detection ability. Two kinds of fiber amplifier, erbium doped fiber amplifier (EDFA) and Raman fiber amplifier (RFA), were combined to amplify the output power of two diode lasers to improve the excitation strength. After optimization, minimum detection limit (MDL) of 268.8 ppb and 91.4 ppb for real-simultaneous CH<sub>4</sub> and C<sub>2</sub>H<sub>2</sub> sensing were obtained, respectively. When the integration time of the system were 150 s and 100 s, the MDLs could be improved to 54.8 ppb and 26.1 ppb, accordingly. Further improvement methods for such sensor were discussed.

**Keywords:** light-induced thermoelectric spectroscopy; Lissajous space-division multiplexed; multi-pass cell; quartz tuning fork; dual-gas sensing

Sun HY, He Y, Qiao SD et al. Highly sensitive and real-simultaneous CH<sub>4</sub>/C<sub>2</sub>H<sub>2</sub> dual-gas LITES sensor based on Lissajous pattern multi-pass cell. *Opto-Electron Sci* **3**, 240013 (2024).

## Introduction

Trace gas detection technology plays an important role in many fields such as environment monitoring and industry process<sup>1-9</sup>. With the advantages of fast response and high sensitivity, laser absorption spectroscopy (LAS) has been researched and applied widely in recent years<sup>10-20</sup>. Two main types of LAS are direct absorption spectroscopy and indirect absorption spectroscopy, which is representative by tunable diode laser absorption spectroscopy (TDLAS) and photoacoustic spectroscopy (PAS), respectively<sup>21,22</sup>. Compared with TDLAS, PAS has no operation laser wavelength limitation due to

its probe object of acoustic wave. In contrast with traditional PAS, quartz-enhanced photoacoustic spectroscopy (QEPAS) replaces the microphone with a quartz tuning fork (QTF) to detect acoustic waves, which is first reported in 2002<sup>23</sup>. Due to the properties of high Q factor, small size and excellent noise suppression of QTF, QEPAS has the merits of high sensitivity and compact size<sup>24-30</sup>. But in the system of QEPAS, QTF needs to be placed in test gas environment, which increases the risk of its corrosion by the corrosive and acid gases<sup>31,32</sup>. In order to solve this problem, light-induced thermoelectric spectroscopy (LITES) was reported by Ma in 2018<sup>33</sup>. In

National Key Laboratory of Laser Spatial Information, Harbin Institute of Technology, Harbin 150000, China.

\*Correspondence: YF Ma, E-mail: [mayufei@hit.edu.cn](mailto:mayufei@hit.edu.cn)

Received: 31 March 2024; Accepted: 24 May 2024; Published online: 28 June 2024



**Open Access** This article is licensed under a Creative Commons Attribution 4.0 International License.

To view a copy of this license, visit <http://creativecommons.org/licenses/by/4.0/>.

© The Author(s) 2024. Published by Institute of Optics and Electronics, Chinese Academy of Sciences.

this technology, the modulation laser passes through the test gas and is focused on the surface of QTF. The light carrying the concentration information of the gas is absorbed by the quartz and converts into a heat signal. Because of the thermal expansion and piezoelectric property of QTF, the heat signal is further converted into an electronic signal to obtain gas concentration information<sup>34–36</sup>. Thus, compared to QEPAS, LITES is a non-contact detection method and is appropriate for various gas sensing<sup>37–40</sup>.

According to the Beer-Lambert law, increasing the optical path length (OPL) can availably improve sensitivity of LITES. Multi-pass cell (MPC) is widely used to increase the effective OPL. Optical path length to volume ratio (OPL/V) is a common indicator for MPC's performance<sup>41–43</sup>. Higher OPL/V means that there is a denser pattern of spot distribution on the mirrors and the system of MPC is more compact. The widely used Herriot MPC can form circular spot patterns by two spherical concave mirrors<sup>44–48</sup>. The projection coordinates of spot patterns on tangential plane and sagittal plane are both distributed to each sine coordinate function. Advance angle in the sine function determines the distance between projection positions. Two-mirror based Herriot MPC has same cavity structures on the orthogonal planes, which results in same advance angles and simple circular patterns. However, spot patterns of two spherical concave mirrors maintain circle symmetries and lack distribution in the center area. Hence, Herriot MPC has a low OPL/V and cannot sustain a compact structure with a long OPL.

Methane (CH<sub>4</sub>) and acetylene (C<sub>2</sub>H<sub>2</sub>) are two important gases in energy and chemical industry. CH<sub>4</sub>, the primary component of natural gas, has as much effect on climate change as carbon dioxide<sup>49,50</sup>. C<sub>2</sub>H<sub>2</sub> is flammable and the leakage of it always leads to serious explosions<sup>51,52</sup>. Therefore, the development of a simultaneous, fast responsive and highly sensitive sensor system for CH<sub>4</sub>/C<sub>2</sub>H<sub>2</sub> has received a lot of attention in recent years<sup>53–55</sup>. For instance, Wang et al. developed a dual-laser sensor based on off-axis cavity-enhanced absorption spectroscopy and time-division multiplexed (TDM) technology in 2020<sup>56</sup>. Raza et al. used frequency-division multiplexed (FDM) to realize simultaneous CH<sub>4</sub>/C<sub>2</sub>H<sub>2</sub> detection in 2022<sup>57</sup>. TDM make each laser operate in separate time and does not provide real-simultaneous detection, so it is difficult to achieve fast response and suit volatile environments. As for FDM, it is unsuitable for

sensor system with resonance frequency, such as QEPAS and LITES. Furthermore, in the above research, light was detected by a photodetector (PD), which has a limited response wavelength range compared to QTF. Recently, double spot-ring Herriot MPC has been used to separating optical paths for double gas detection in TDLAS<sup>58,59</sup>. However, this scheme faces two issues: 1) The circular pattern results in less efficient use of the central area of the mirror surface. 2) For the same optical path length, the overall size of the system is determined by the outer large ring, leading to an increased system volume. To address these issues, Lissajous spot patterns for optical path separation in LITES technology was adopted in this research.

In this paper, we present a highly sensitive and real-simultaneous CH<sub>4</sub>/C<sub>2</sub>H<sub>2</sub> dual-gas LITES sensor based on a novel Lissajous space-division multiplexed (LSDM) MPC and trapezoidal-head QTF. An additional mirror was added to the two-mirror cavity to form a three-mirror based cavity with different advance angles on the orthogonal planes. Sine functions with different advance angles in tangential plane and sagittal plane was combined to form a pair of complementary Lissajous spot patterns with high OPL/V. The MPC with a small volume of 67.5 mL has two OPLs of 9.1 m and 9.0 m in a cavity to enhance absorption of the dual-gas. Two self-designed trapezoidal-head QTFs with low resonant frequencies were used to improve the detection performance of the LSDM-MPC based LITES sensor system.

## Experimental setup

### Principle of three-mirror MPC with dual-path

As shown in Fig. 1, the self-designed MPC consisted of three spherical mirrors with curvatures of  $R$ . Mirrors (M1, M2 and M3) were cut into same rectangle and placed around the  $x$  axis to constitute a circular cavity. Long side ( $L$ ) and wide side ( $W$ ) of mirrors were located in  $y$ - $z$  plane and parallel to  $x$  axis, respectively. Distance from mirror to the origin and angle between mirrors were presented by  $d$  ( $d_1$ ,  $d_2$  and  $d_3$ ) and  $\alpha$  ( $\alpha_1$  and  $\alpha_2$ ), respectively. The angle of incident laser can be determined by  $\theta$  and  $\varphi$ . The incident light entering through the hole on M1 was reflected by M2, M3 and M1 in turn to complete a ring path.

The analytical method of vector ray tracing was suitable for the complex three-mirror MPC.  $P_i$  and  $N$  represented the spatial coordinates of the  $i^{\text{th}}$  ( $i = 1, 2, \dots, N$ ) light

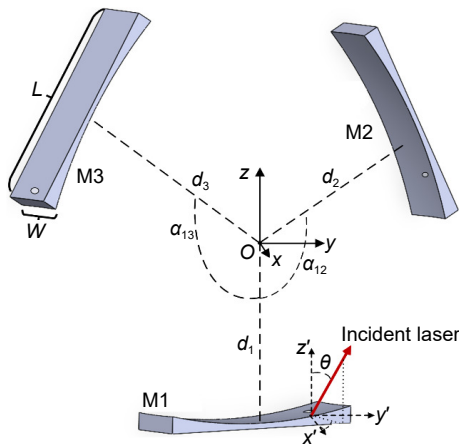


**Fig. 1 | Structure diagram of three-mirror astigmatic MPC.** *L*: long side of mirrors; *W*: wide side of mirrors; *d*: distance from mirror to the origin;  $\alpha$ : angle between mirrors;  $\theta$ : the angle between the incident laser and the *z* axis;  $\varphi$ : the angle between the projection of the incident ray in the *x-y* plane and the *x* axis.

spot and its total number including the entry and exit holes on mirrors, respectively. The coordinates could be expressed as:

$$P_{i+1} = P_i + L_i \cdot P_{i(i+1)}, \quad (1)$$

$$P_{(i+1)(i+2)} = P_{i(i+1)} - 2(P_{i(i+1)} \cdot n_i) \cdot n_i, \quad (2)$$

$$n_i = \frac{P_i - r_i}{R}, \quad (3)$$

$$L_i = -n_i \cdot (P_i - r_i) + \sqrt{(n_i \cdot (P_i - r_i))^2 - (P_i - r_i) \cdot (P_i - r_i) + R^2}, \quad (4)$$

where  $P_{i(i+1)}$  and  $n_i$  represented normal direction vector of the  $i^{\text{th}}$  ray and normal vector of the sphere at the  $i^{\text{th}}$  spot, respectively.  $r_i$  represented the center of the sphere mirrors and could be expressed as:

$$r_i = \begin{cases} (0, 0, R - d_1)', & i = 1, 4, 7, \dots \\ \mathbf{R}_m(\alpha_{12}) \cdot (0, 0, R - d_2)', & i = 2, 5, 8, \dots \\ \mathbf{R}_m(-\alpha_{13}) \cdot (0, 0, R - d_3)', & i = 3, 6, 9, \dots \end{cases}, \quad (5)$$

where  $\mathbf{R}_m$ , the anticlockwise rotation matrix of the three-mirror system, was described below:

$$\mathbf{R}_m = \begin{bmatrix} 1 & 0 & 0 \\ 0 & \cos\alpha & -\sin\alpha \\ 0 & \sin\alpha & \cos\alpha \end{bmatrix}. \quad (6)$$

According to the above equations, the specific coordinates of the light spots on mirrors could be iteratively calculated. The side lengths of rectangular mirrors were 12 mm and 44 mm, respectively. Each mirror had a hole with diameter of 2 mm. In order to realize LSDM, double lights entered through a same hole (h1) in M1 and exited through different holes (h2 and h3) in M2 and M3, respectively. The double lights were used to detect  $\text{CH}_4/\text{C}_2\text{H}_2$  simultaneously. By optimizing the parameters of the incident lights and positions of mirrors, non-axisymmetric tilted three-ring Lissajous pattern was formed on mirrors. Because the system was symmetric to the *x-z* plane, incident beams with opposite directions in *x* axis could form a pair of mirror patterns. In this way, we obtained complementary Lissajous patterns shown in Fig. 2(a) and the corresponding parameters were listed in Table 1.

The MPC adopted off-center incident laser and non-equidistant mirrors, which could reduce angle  $\theta$  and then was in favor of low occlusion loss caused by h1. The optimization of  $\alpha$  could decrease the distribution shift of the Lissajous patterns resulted from non-equidistant mirrors. As illustrated in Fig. 2(b), high-precision guide rails were machined onto the installation platform. The guide rails and the installation platform were integrally machined by computerized numerical control (CNC) to minimize sources of error. The tolerance for the positional accuracy of the guide rails could be maintained within  $\pm 0.2$  mm. Adjusting the mirror along the guide rails allowed us to reduce the original multiple dimensions of adjustment to a single dimension. Measurements

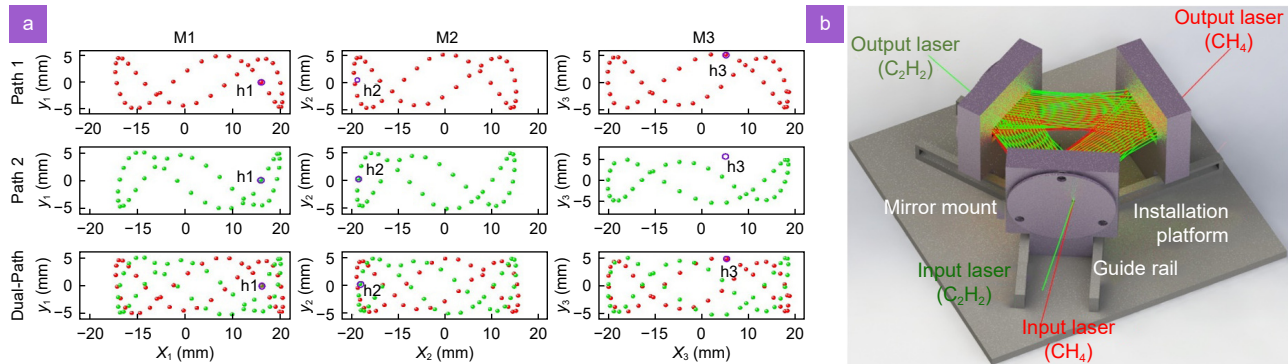


**Fig. 2 | (a)** Simulated results of dual-path Lissajous patterns on three mirrors. **(b)** The diagram of double optical paths in Lissajous patterns MPC.



**Table 1 | Parameters of three-mirror MPC with dual-path.**

Path	$x_0, y_0$ (mm)	$\theta, \varphi$ (°)	$d_1, d_2, d_3$ (mm)	$\alpha_{12}, \alpha_{13}$ (°)	$N$	OPL (m)	V (mL)	OPL/V (cm <sup>-2</sup> )
1	15.8, 0	13.5, 77	42, 41, 49.9	118, 121	120	9.1	67.5	13.5
2	15.8, 0	13, 103	42, 41, 49.9	118, 121	119	9.0	67.5	13.3

and adjustments were made using a digital high-precision caliper to gauge the mirror mount's position relative to the top of the guide rail. The relative accuracy was dependent on the digital caliper and could be ensured within  $\pm 0.03$  mm.

Finally, the dual-path astigmatic MPC based on three mirrors was successfully demonstrated for the first time. The real distribution of light spots obtained with red/green diode lasers was shown in Fig. 3. The mirrors employed were silver-coated with the reflectivity rate of 98%. The beam of path 1 was reflected for 120 times and exited from h3 with OPL of 9.14 m. Another beam of path 2 sharing same cavity was reflected for 119 times and exited early from h2 with OPL of 9.04 m. The volume of the optical system and the total OPL/V were 67.5 mL and 27 cm<sup>-2</sup>, respectively. OPL/V ratio serves as a comprehensive metric for assessing the compactness of the multi-pass cell and the length of the optical path. It is also an important criterion for the overall evaluation of the detection sensitivity and volume of the entire sensing system. Current reports on multi-pass cells primarily

focus on designing such as two-spherical-mirror MPCs with different patterns and toroidal MPCs. The specifications for these multi-pass cells are shown in Table 2. The self-designed Lissajous pattern multi-pass cell with two independent light paths and compact structure could be utilized to achieve highly sensitive and real-simultaneous detection of dual-gas.

### CH<sub>4</sub>/C<sub>2</sub>H<sub>2</sub> dual-gas LITES sensor based on LSDM MPC and trapezoidal-head QTF

Schematic diagram of real-simultaneous dual-gas LITES sensor based on LSDM-MPC is shown in Fig. 4. Two absorption lines of CH<sub>4</sub> and C<sub>2</sub>H<sub>2</sub> located at 1650.96 nm (6057.08 cm<sup>-1</sup>) and 1530.37 nm (6534.37 cm<sup>-1</sup>), respectively, were chosen in the sensor system. Distributed feedback (DFB) diode laser 1 and diode laser 2 with maximum output power of 28 mW and 21 mW were used as the light source to detect CH<sub>4</sub> and C<sub>2</sub>H<sub>2</sub>, respectively. Fiber amplifiers were adopted to amplify the laser output power. Raman fiber amplifier (RFA) was selected to amplify the maximum output power of DFB diode laser

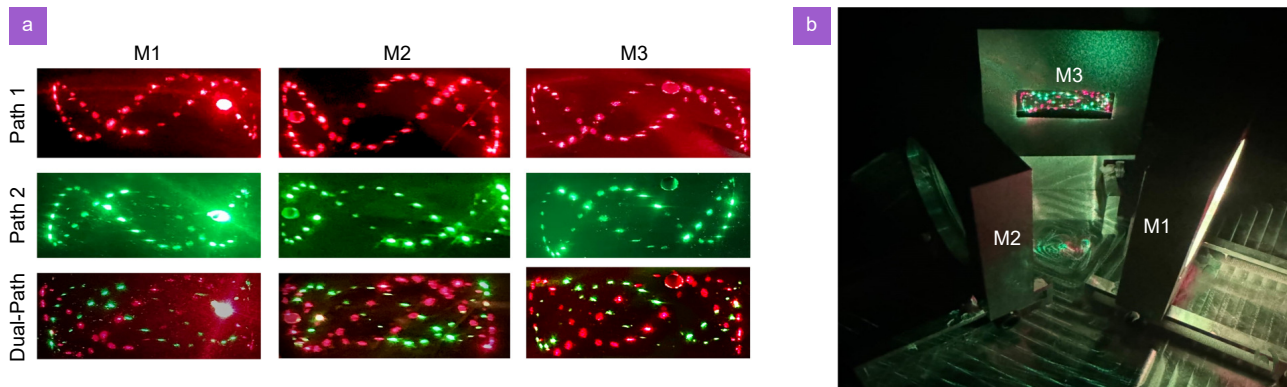


**Fig. 3 | (a)** Measured distribution of dual-path Lissajous patterns on three mirrors. **(b)** The picture of the three mirrors MPC with dual-path Lissajous pattern.

**Table 2 | Parameters comparison between reported MPCs and Lissajous space-division MPC.**

Types of MPC	$N$	OPL (m)	V (mL)	Total OPL/V (cm <sup>-2</sup> )
Seven-circle spot pattern MPC <sup>60</sup>	215	26.4	249	11
Nine-circle spot pattern MPC <sup>61</sup>	235	32.66	281.71	11.59
Triangular spot pattern MPC <sup>62</sup>	138	14.6	330.0	4.42
Petal spot pattern MPC <sup>62</sup>	183	20.4	332.1	6.14
Toroidal MPC <sup>63</sup>	51	4.1	40	10.3
Segmented circular MPC <sup>64</sup>	64	9.89	140	7
Lissajous space-division MPC (this paper)	120, 121	9, 9.1	67.5	26.8

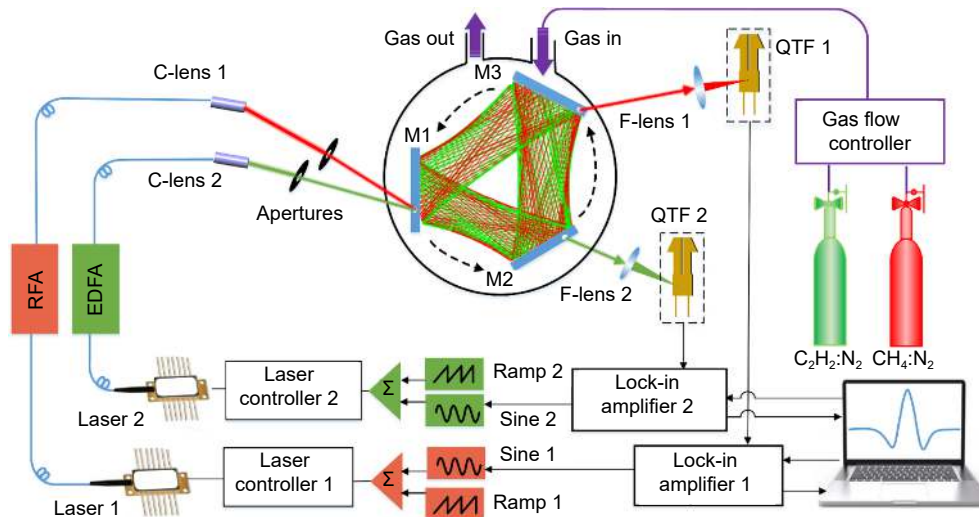


**Fig. 4 |** Schematic diagram of simultaneous  $\text{CH}_4/\text{C}_2\text{H}_2$  dual-gas LITES sensor based on LSDM-MPC and trapezoidal-head QTF. RFA: Raman fiber amplifier; EDFA: Erbium doped fiber amplifier; C-lens: collimating lens; F-lens: focusing lenses; QTF: quartz tuning fork.

1 to 300 mW, ensuring a single-longitudinal-mode operation. Erbium doped fiber amplifier (EDFA) with maximum output power of 1000 mW was employed to amplify the output power of DFB diode laser 2. Two laser beams were collimated by collimating lenses (C-lenses) and entered into the MPC. Apertures were used to decreased diameters of light spots. After multiple reflections by three mirrors, double beams exited from different mirrors (M2 and M3) and then were focused on center of the corresponding QTF's root, respectively. The focal lengths of focusing lenses (F-lenses) were both 8 mm. Wavelength modulation spectroscopy (WMS) was adopted in this system to suppress the background noise. Sine and sawtooth waves produced from lock-in amplifiers were used to modulate the laser wavelength. Sine

sawtooth wave's scanning frequency was set to 100 mHz. Finally, the generated piezoelectric signals were demodulated by the lock-in amplifiers, which was configured with an integration time of 10 ms.

## Results and discussion

Firstly, the performance of LSDM-MPC was checked by direct absorption measurement and replacing QTFs with PDs. Concentrations of  $\text{CH}_4$  and  $\text{C}_2\text{H}_2$  in LSDM MPC were both 200 ppm. When the injection current of laser 1 was scanned across the absorption line of  $\text{CH}_4$ , only PD1 could detect a significant electronic signal. According to the absorption peak of  $\text{CH}_4$ , the absorbance was calculated to be 0.08. Conversely, when the scanning signal was injected into laser 2, only PD2 could detect an

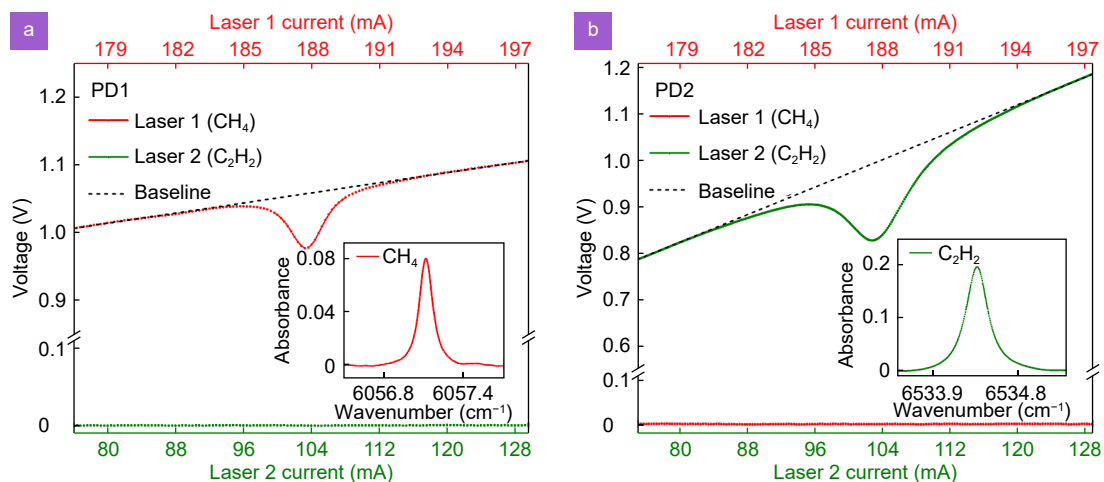


**Fig. 5 |** (a) The responses of PD1 to path 1 and path 2, respectively. Insert: The absorbance of 200 ppm  $\text{CH}_4$  at  $6057.08\text{ cm}^{-1}$ . (b) The responses of PD2 to path 1 and path 2, respectively. Insert: The absorbance of 200 ppm  $\text{C}_2\text{H}_2$  at  $6534.37\text{ cm}^{-1}$ .

obvious electronic signal and the absorbance of  $C_2H_2$  was calculated to be 0.20. As shown in Fig. 5, there wasn't significant crosswalk between the double paths. After removing the absorption peak from spectrum, a linear fit was adapted to approximate the baseline based on the remaining data. Based on the absorbance, OPLs of path 1 and path 2 were determined to be 9.1 m and 8.9 m. Theoretical value for the path 2 was 9.0 m, indicating a deviation error of 1.1% within an acceptable range.

Usually in LITES sensor, commercially available QTF with silver coating and resonant frequency of 32.768 kHz is adopted. In order to improve the conversion efficiency of light-induced thermoelectric, a novel trapezoidal-head QTF with gold coating was designed in the research. The gold electrode allowed for a reduction in electrode resistance and improvement on the corrosion resistance. Additionally, gold electrodes can also improve the corrosion resistance of the tuning fork. Parameters of the novel QTFs were optimized by finite element analysis to achieve a lower resonant frequency, maximize the average charge density, and enhance the surface stress for improved performance. The resonant frequencies of trapezoidal-head QTF1 and QTF2 were measured as 9451.49 Hz and 9464.15 Hz, respectively, as shown in Fig. 6. The frequency deviation of the novel QTFs were caused by minor discrepancies in the dimensional processing. The quality factor (Q) for the two QTFs were determined as 11387.7 and 12452.8, respectively. Compared with high resonant frequency of 32.768 kHz of commercial QTF, low resonant frequency of the self-designed trapezoidal-head QTF is conducive to rise energy accumulation time and therefore could improve piezoelectric conversion performance of the QTF.

Modulation depths of  $CH_4/C_2H_2$  dual-gas sensing

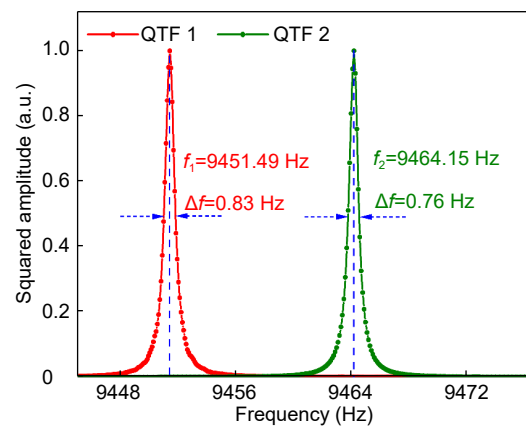


**Fig. 6 |** Frequency response of the trapezoidal-head QTF1 and QTF2 in the dual-gas LITES sensor.

were optimized in the WMS technique. As shown in Fig. 7, the optimum  $2f$  signals of  $CH_4$  and  $C_2H_2$  were obtained with modulation depths of 5.13 mA and 14.85 mA, respectively. RFA and EDFA were used to boost the optical power of the two diode lasers. The relationships between  $2f$  peak values and output power of fiber amplifiers at optimum modulation depths were investigated and are shown in Fig. 8. Concentrations of  $CH_4$  and  $C_2H_2$  were both set to 200 ppm. It can be seen that  $2f$  peak values increased linearly with the output power and reached the highest when the output power of RFA and EDFA were set to the maximum 300 mW and 1000 mW, respectively. After linear fitting, the R-square value of 0.99 was obtained for both sensing system, which indicated the  $CH_4/C_2H_2$  dual-gas LITES sensor based on LS-DM-MPC and trapezoidal-head QTF had excellent power response. Noise standard deviations and signal to noise ratio (SNR) with different output powers of RFA and EDFA were measured and are depicted in Fig. 9. The

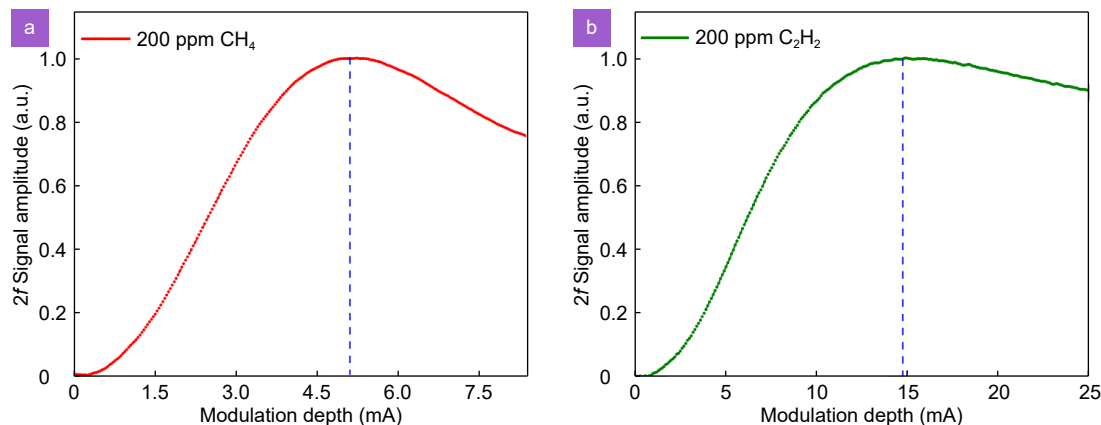


**Fig. 7 |** (a)  $2f$  signal amplitude of 200 ppm  $CH_4$  with different modulation depth based LITES sensor. (b)  $2f$  signal amplitude of 200 ppm  $C_2H_2$  with different modulation depth based LITES sensor.

best SNR of CH<sub>4</sub> and C<sub>2</sub>H<sub>2</sub> detections were calculated to be 744.1 and 2187.3 with the maximum output powers, and corresponding minimum detection limits (MDLs) were determined to be 268.8 ppb and 91.4 ppb, respectively.

The relationship between the 2f signal values and various concentrations of double gases were researched si-

multaneously and is displayed in Fig. 10. Two flowmeters were used to control the flow speed of CH<sub>4</sub> and C<sub>2</sub>H<sub>2</sub> standard gases to adjust the concentrations of the double gases in MPC. The experimental results indicated that two signals of CH<sub>4</sub> and C<sub>2</sub>H<sub>2</sub> were proportional to each concentration. Corresponding values of R-square after linear fitting were both 0.99, indicating an excellent

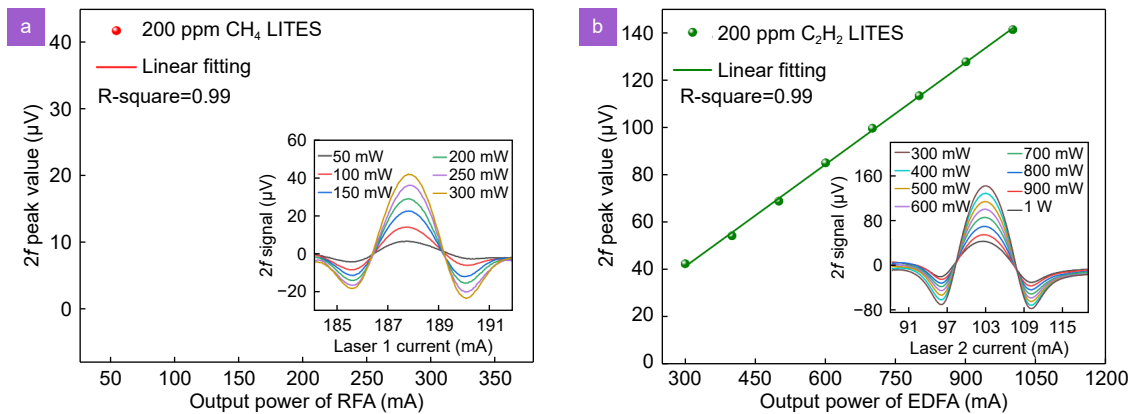


**Fig. 8 |** (a) Relationship between 2f peak value of CH<sub>4</sub> LITES and output power of RFA. Insert: 2f WMS signal waveform of CH<sub>4</sub>. (b) Relationship between 2f signal amplitude of C<sub>2</sub>H<sub>2</sub> LITES and output power of EDFA. Insert: 2f WMS signal waveform of C<sub>2</sub>H<sub>2</sub>.

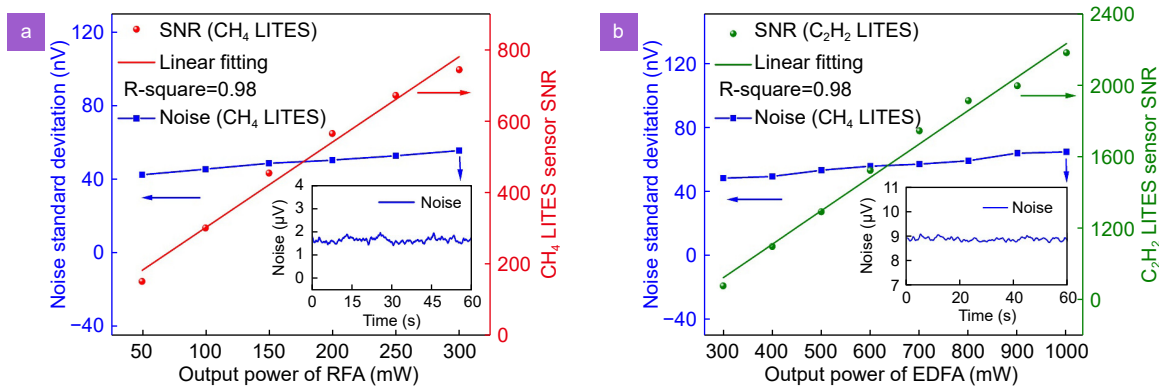


**Fig. 9 |** (a) Noise level and SNR of CH<sub>4</sub> detection with different output power of RFA. Insert: Noise signal at maximum output power of RFA. (b) Noise level and SNR of C<sub>2</sub>H<sub>2</sub> detection with different output power of EDFA. Insert: Noise signal at maximum output power of EDFA.

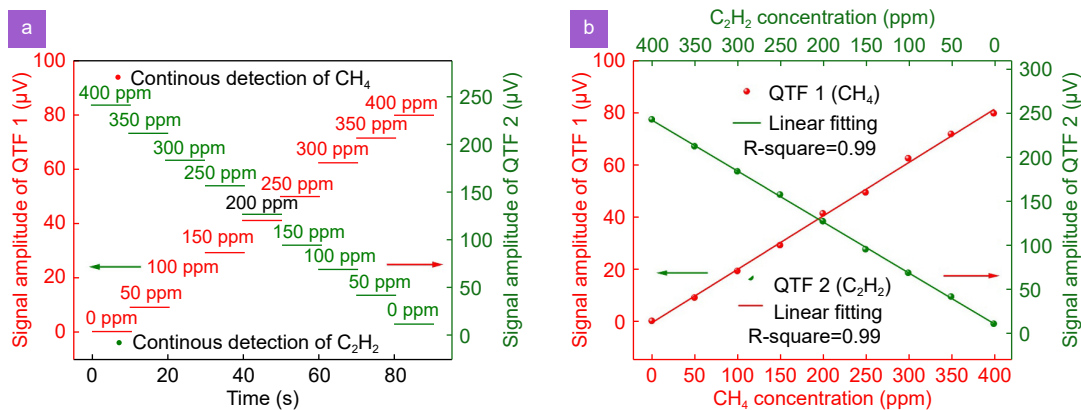


**Fig. 10 |** (a) Concentration responses of dual-gas LITES sensor based on LSDM-MPC and trapezoidal-head QTF. (b) The linear relationship between 2f signal amplitude and concentration of CH<sub>4</sub> and C<sub>2</sub>H<sub>2</sub>.



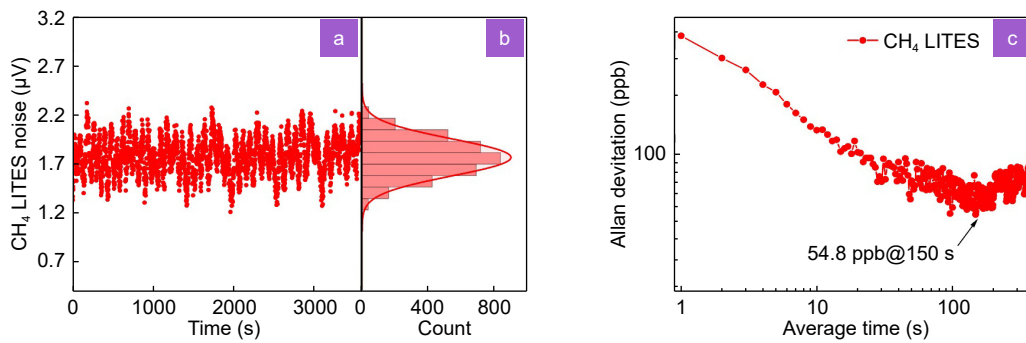


**Fig. 11** | (a) Continuous noise detection in CH<sub>4</sub> LITES sensor. (b) Normal distribution of experimental points for noise detection. (c) Allan variance analysis of path 1 for CH<sub>4</sub> detection.

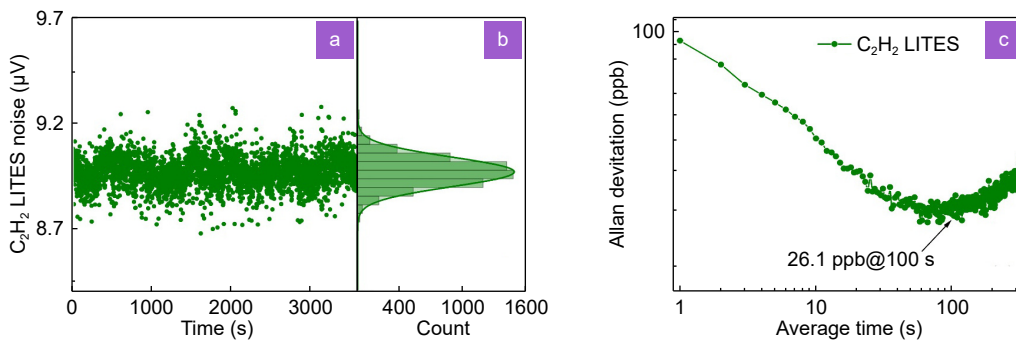


**Fig. 12** | (a) Continuous noise detection in C<sub>2</sub>H<sub>2</sub> LITES sensor. (b) Normal distribution of experimental points for noise detection. (c) Allan variance analysis of path 2 for C<sub>2</sub>H<sub>2</sub> detection.

linear concentration response. Allan deviation analysis was used to investigate the long-term stability of the system. Pure nitrogen (N<sub>2</sub>) was flushed into the LSDM-MPC. As shown in Fig. 11 and Fig. 12, when the integration time were 150 s and 100 s, the MDLs of CH<sub>4</sub> and C<sub>2</sub>H<sub>2</sub> detections were improved to 26.1 ppb and 54.8 ppb, respectively.

## Conclusion

In this paper, a highly sensitive and real-simultaneous CH<sub>4</sub>/C<sub>2</sub>H<sub>2</sub> dual-gas LITES sensor based on a novel LSDM-MPC and trapezoidal-head QTF was demonstrated for the first time. A theoretical model was established on the basis of three-mirror astigmatic MPC to realized LSDM technique, and a pair of Lissajous spot patterns with OPLs of 9.1 m and 9.0 m and OPL/Vs of 13.5 cm<sup>-2</sup> and 13.3 cm<sup>-2</sup> were obtained respectively. Two trapezoidal-head QTFs with low resonant frequencies of ~9.4 kHz and Q factor as high as ~12000 were designed and adopted to enhance the energy accumulation time and LITES sensor detection ability. Two fiber amplifiers RFA and EDFA were employed to amplify the optical power of excitation source diode lasers to 300 mW and 1000 mW, respectively. Excellent concentration linear response was

obtained for continuous and simultaneous monitoring of dual-gas in LITES sensor based on LSDM-MPC and trapezoidal-head QTF. Finally, MDLs for real-simultaneous CH<sub>4</sub>/C<sub>2</sub>H<sub>2</sub> detections were measured to be 268.8 ppb and 91.4 ppb, respectively. When the integration times of the system were increased to 150 s and 100 s, the MDLs could be improved to 54.8 ppb and 26.1 ppb, accordingly. The performance of the dual-gas LITES sensor based on LSDM-MPC can be improved in further when mirrors with higher reflectivity (>99%) are adopted in MPC. In addition, utilizing lasers operated in mid-infrared absorption bands, QTF with photothermally enhanced coating or transimpedance amplification of the electrical signal, could further enhance the detector's sensitivity.

## References

1. Leal-Junior A, Avellar L, Biazzi V et al. Multifunctional flexible optical waveguide sensor: on the bioinspiration for ultrasensitive sensors development. *Opto-Electron Adv* 5, 210098 (2022).
2. Dong L, Li CG, Sanchez NP et al. Compact CH<sub>4</sub> sensor system based on a continuous-wave, low power consumption, room temperature interband cascade laser. *Appl Phys Lett* 108, 011106 (2016).
3. Wan F, Wang R, Ge H et al. Optical feedback frequency locking: impact of directly reflected field and responding strategies. *Opt Express* 32, 12428–12437 (2024).

4. Xu BX, Fan XY, Wang S et al. Sub-femtometer-resolution absolute spectroscopy with sweeping electro-optic combs. *Opto-Electron Adv* 5, 210023 (2022).
5. Zhang ZD, Peng T, Nie XY et al. Entangled photons enabled time-frequency-resolved coherent Raman spectroscopy and applications to electronic coherences at femtosecond scale. *Light Sci Appl* 11, 274 (2022).
6. Jiang SL, Chen FF, Zhao Y et al. Broadband all-fiber optical phase modulator based on photo-thermal effect in a gas-filled hollow-core fiber. *Opto-Electron Adv* 6, 220085 (2023).
7. Hou JF, Liu XN, Liu YH et al. Highly sensitive CO<sub>2</sub>-LITES sensor based on a self-designed low-frequency quartz tuning fork and fiber-coupled MPC. *Chin Opt Lett* 22, 073001 (2024).
8. Zheng ZH, Zhu SK, Chen Y et al. Towards integrated mode-division demultiplexing spectrometer by deep learning. *Opto-Electron Sci* 1, 220012 (2022).
9. Qiao SD, He Y, Sun HY et al. Ultra-highly sensitive dual gases detection based on photoacoustic spectroscopy by exploiting a long-wave, high-power, wide-tunable, single-longitudinal-mode solid-state laser. *Light Sci Appl* 13, 100 (2024).
10. Li DR, Wang NN, Zhang TY et al. Label-free fiber nanograting sensor for real-time in situ early monitoring of cellular apoptosis. *Adv Photonics* 4, 016001 (2022).
11. Lang ZT, Qiao SD, Ma YF. Fabry-Perot-based phase demodulation of heterodyne light-induced thermoelastic spectroscopy. *Light Adv Manuf* 4, 233-242 (2023).
12. Wang XY, Qiu XK, Liu ML et al. Flat soliton microcomb source. *Opto-Electron Sci* 2, 230024 (2023).
13. Zhang L, Zhang M, Chen TN et al. Ultrahigh-resolution on-chip spectrometer with silicon photonic resonators. *Opto-Electron Adv* 5, 210100 (2022).
14. Sun WF, Wang XK, Zhang Y. Terahertz generation from laser-induced plasma. *Opto-Electron Sci* 1, 220003 (2022).
15. Liu XN, Ma YF. New temperature measurement method based on light-induced thermoelastic spectroscopy. *Opt Lett* 48, 5687–5690 (2023).
16. Chen WP, Qiao SD, He Y et al. Mid-infrared all-fiber light-induced thermoelastic spectroscopy sensor based on hollow-core anti-resonant fiber. *Photoacoustics* 36, 100594 (2024).
17. Hashimoto K, Nakamura T, Kageyama T et al. Upconversion time-stretch infrared spectroscopy. *Light Sci Appl* 12, 48 (2023).
18. Zhang C, Qiao SD, He Y et al. Trace gas sensor based on a multi-pass-retro-reflection-enhanced differential Helmholtz photoacoustic cell and a power amplified diode laser. *Opt Express* 32, 848–856 (2024).
19. Wang YQ, Zhang JH, Zheng YC et al. Brillouin scattering spectrum for liquid detection and applications in oceanography. *Opto-Electron Adv* 6, 220016 (2023).
20. Gao H, Fan XH, Wang YX et al. Multi-foci metalens for spectra and polarization ellipticity recognition and reconstruction. *Opto-Electron Sci* 2, 220026 (2023).
21. Shao LG, Fang B, Zheng F et al. Simultaneous detection of atmospheric CO and CH<sub>4</sub> based on TDLAS using a single 2.3 μm DFB laser. *Spectrochim Acta A Mol Biomol Spectrosc* 222, 117118 (2019).
22. Zhang C, He Y, Qiao SD et al. Differential integrating sphere-based photoacoustic spectroscopy gas sensing. *Opt Lett* 48, 5089–5092 (2023).
23. Kosterev AA, Bakhrkin YA, Curl RF et al. Quartz-enhanced photoacoustic spectroscopy. *Opt Lett* 27, 1902–1904 (2002).
24. Li B, Feng CF, Wu HP et al. Calibration-free mid-infrared exhaled breath sensor based on BF-QEPAS for real-time ammonia measurements at ppb level. *Sens Actuators B Chem* 358, 131510 (2022).
25. Chen WP, Qiao SD, Lang ZT et al. Hollow-waveguide-based light-induced thermoelastic spectroscopy sensing. *Opt Lett* 48, 3989–3992 (2023).
26. Menduni G, Zifarelli A, Sampaolo A et al. High-concentration methane and ethane QEPAS detection employing partial least squares regression to filter out energy relaxation dependence on gas matrix composition. *Photoacoustics* 26, 100349 (2022).
27. Ma YF, Lewicki R, Razeghi M et al. QEPAS based ppb-level detection of CO and N<sub>2</sub>O using a high power CW DFB-QCL. *Opt Express* 21, 1008–1019 (2013).
28. Shi C, Wang DE, Wang Z et al. A mid-infrared fiber-coupled QEPAS nitric oxide sensor for real-time engine exhaust monitoring. *IEEE Sens J* 17, 7418–7424 (2017).
29. Lang ZT, Qiao SD, Liang TT et al. Dual-frequency modulated heterodyne quartz-enhanced photoacoustic spectroscopy. *Opt Express* 32, 379–386 (2024).
30. Chao F, Liang TT, Qiao SD et al. Quartz-enhanced photoacoustic spectroscopy sensing using trapezoidal- and round-head quartz tuning forks. *Opt Lett* 49, 770–773 (2024).
31. Ma YF, He Y, Yu X et al. HCl ppb-level detection based on QEPAS sensor using a low resonance frequency quartz tuning fork. *Sens Actuators B Chem* 233, 388–393 (2016).
32. Wu HP, Sampaolo A, Dong L et al. Quartz enhanced photoacoustic H<sub>2</sub>S gas sensor based on a fiber-amplifier source and a custom tuning fork with large prong spacing. *Appl Phys Lett* 107, 111104 (2015).
33. Ma YF, He Y, Tong Y et al. Quartz-tuning-fork enhanced photoacoustic spectroscopy for ultra-high sensitive trace gas detection. *Opt Express* 26, 32103–32110 (2018).
34. Liu XN, Qiao SD, Ma YF. Highly sensitive methane detection based on light-induced thermoelastic spectroscopy with a 2.33 μm diode laser and adaptive Savitzky-Golay filtering. *Opt Express* 30, 1304–1313 (2022).
35. Wu Q, Lv HH, Li JM et al. Side-excitation light-induced thermoelastic spectroscopy. *Opt Lett* 48, 562–565 (2023).
36. Ma YF, Liang TT, Qiao SD et al. Highly sensitive and fast hydrogen detection based on light-induced thermoelastic spectroscopy. *Ultrafast Sci* 3, 0024 (2023).
37. Sun B, Patimisco P, Sampaolo A et al. Light-induced thermoelastic sensor for ppb-level H<sub>2</sub>S detection in a SF<sub>6</sub> gas matrices exploiting a mini-multi-pass cell and quartz tuning fork photodetector. *Photoacoustics* 33, 100553 (2023).
38. Liu XN, Ma YF. Sensitive carbon monoxide detection based on light-induced thermoelastic spectroscopy with a fiber-coupled multipass cell [Invited]. *Chin Opt Lett* 20, 031201 (2022).
39. Hu LE, Zheng CT, Zhang MH et al. Long-distance in-situ methane detection using near-infrared light-induced thermoelastic spectroscopy. *Photoacoustics* 21, 100230 (2021).
40. Hudzikowski A, Gluszek A, Krzempek K et al. Compact, spherical mirror-based dense astigmatic-like pattern multipass cell design aided by a genetic algorithm. *Opt Express* 29, 26127–26136 (2021).
41. He Y, Ma YF, Tong Y et al. Ultra-high sensitive light-induced thermoelastic spectroscopy sensor with a high Q-factor quartz tuning fork and a multipass cell. *Opt Lett* 44, 1904–1907 (2019).
42. Liu YH, Qiao SD, Fang C et al. A highly sensitive LITES sensor

- based on a multi-pass cell with dense spot pattern and a novel quartz tuning fork with low frequency. *Opto-Electron Adv* 7, 230230 (2024).
43. Liu YH, Ma YF. Advances in multipass cell for absorption spectroscopy-based trace gas sensing technology [Invited]. *Chin Opt Lett* 21, 033001 (2023).
  44. Engel GS, Moyer EJ. Precise multipass Herriott cell design: derivation of controlling design equations. *Opt Lett* 32, 704–706 (2007).
  45. Li CL, Liu LL, Qiu XB et al. Optical heterodyne Herriott-type multipass laser absorption spectrometer. *Chin Opt Lett* 13, 013001 (2015).
  46. Tarsitano CG, Webster CR. Multilaser Herriott cell for planetary tunable laser spectrometers. *Appl Opt* 46, 6923–6935 (2007).
  47. Han X, Li CX, Guo M et al. Fiber-optic trace gas sensing based on graphite excited photoacoustic wave. *Sens Actuators B Chem* 408, 135546 (2024).
  48. McManus JB, Kebabian PL, Zahniser MS. Astigmatic mirror multipass absorption cells for long-path-length spectroscopy. *Appl Opt* 34, 3336–3348 (1995).
  49. De Geyter C, Van de Maele K, Hauser B et al. Hydrogen and methane breath test in the diagnosis of lactose intolerance. *Nutrients* 13, 3261 (2021).
  50. Liang TT, Qiao SD, Chen YJ et al. High-sensitivity methane detection based on QEPAS and H-QEPAS technologies combined with a self-designed 8.7 kHz quartz tuning fork. *Photoacoustics* 36, 100592 (2024).
  51. Marshall ST, Schwartz DK, Medlin JW. Selective acetylene detection through surface modification of metal–insulator–semiconductor sensors with alkanethiolate monolayers. *Sens Actuators B Chem* 136, 315–319 (2009).
  52. Miller KL, Morrison E, Marshall ST et al. Experimental and modeling studies of acetylene detection in hydrogen/acetylene mixtures on PdM bimetallic metal–insulator–semiconductor devices. *Sens Actuators B Chem* 156, 924–931 (2011).
  53. Zhang LW, Zhang ZR, Sun PS et al. A dual-gas sensor for simultaneous detection of methane and acetylene based on time-sharing scanning assisted wavelength modulation spectroscopy. *Spectrochim Acta A Mol Biomol Spectrosc* 239, 118495 (2020).
  54. Zheng KY, Zheng CT, Yao D et al. A near-infrared C<sub>2</sub>H<sub>2</sub>/CH<sub>4</sub> dual-gas sensor system combining off-axis integrated-cavity output spectroscopy and frequency-division-multiplexing-based wavelength modulation spectroscopy. *Analyst* 144, 2003–2010 (2019).
  55. Ye WL, Xia ZK, Hu LE et al. Infrared dual-gas CH<sub>4</sub>/C<sub>2</sub>H<sub>2</sub> sensor system based on dual-channel off-beam quartz-enhanced photoacoustic spectroscopy and time-division multiplexing technique. *Spectrochim Acta A Mol Biomol Spectrosc* 285, 121908 (2023).
  56. Wang KY, Shao LG, Chen JJ et al. A dual-laser sensor based on off-axis integrated cavity output spectroscopy and time-division multiplexing method. *Sensors* 20, 6192 (2020).
  57. Raza M, Xu K, Lu ZM et al. Simultaneous methane and acetylene detection using frequency-division multiplexed laser absorption spectroscopy. *Opt Laser Technol* 154, 108285 (2022).
  58. Dong M, Zheng CT, Yao D et al. Double-range near-infrared acetylene detection using a dual spot-ring Herriott cell (DSR-HC). *Opt Express* 26, 12081–12091 (2018).
  59. Hu Z, Shi YP, Niu MS et al. Near-infrared dual-gas sensor for simultaneous detection of CO and CH<sub>4</sub> using a double spot-ring plane-concave multipass cell and a digital laser frequency stabilization system. *Opt Express* 32, 14169–14186 (2024).
  60. Liu K, Wang L, Tan T et al. Highly sensitive detection of methane by near-infrared laser absorption spectroscopy using a compact dense-pattern multipass cell. *Sens Actuators B Chem* 220, 1000–1005 (2015).
  61. Cui RY, Dong L, Wu HP et al. Generalized optical design of two-spherical-mirror multi-pass cells with dense multi-circle spot patterns. *Appl Phys Lett* 116, 091103 (2020).
  62. Kong R, Sun T, Liu P et al. Optical design and analysis of a two-spherical-mirror-based multipass cell. *Appl Opt* 59, 1545–1552 (2020).
  63. Tuzson B, Mangold M, Looser H et al. Compact multipass optical cell for laser spectroscopy. *Opt Lett* 38, 257–259 (2013).
  64. Graf M, Emmenegger L, Tuzson B. Compact, circular, and optically stable multipass cell for mobile laser absorption spectroscopy. *Opt Lett* 43, 2434–2437 (2018).

## Acknowledgements

National Natural Science Foundation of China (Grant No. 62335006, 62022032, 62275065, and 61875047), Key Laboratory of Opto-Electronic Information Acquisition and Manipulation (Anhui University), Ministry of Education (Grant No. OEIAM202202), Fundamental Research Funds for the Central Universities (Grant No. HIT.OCEF.2023011).

## Author contributions

YF Ma proposed the original idea, supervised the whole project and revised the manuscript. HY Sun performed the measurements and wrote the original manuscript. YF Ma, HY Sun, Y He, SD Qiao and YH Liu involved in the investigations.

## Competing interests

The authors declare no competing financial interests.



Scan for Article PDF